DOI: 10.1002/adem. 201600807

Microstructure and Corrosion Behavior of the Friction Stir Welded Joints Made from Ultrafine Grained Aluminium

By *Marta Lipińska**, *Ewa Ura-Bińczyk, Lech Olejnik, Andrzej Rosochowski, Małgorzata Lewandowska*

[*] *M. Lipińska, Dr. Ewa Ura-Bińczyk, Prof. Małgorzata Lewandowska*

Faculty of Materials Science and Engineering, Warsaw University of Technology, Woloska 141, 02-507 Warsaw, Poland

E-mail: marta.lipinska@inmat.pw.edu.pl

Dr. Lech Olejnik

Institute of Manufacturing Processes, Warsaw University of Technology, Narbutta 85, 02-524 Warsaw, Poland

Dr. Andrzej Rosochowski

Design, Manufacture and Engineering Management, University of Strathclyde, 75 Montrose Street, Glasgow G1 1XJ, United Kingdom

[**] Authors would like to acknowledge the financial support by the National Centre for Research and Development of Poland within the project “Properties and longterm behaviour of dissimilar joints of advanced materials for lightweight structures in energy saving applications” (Grant Agreement No. WPN/6/2013). Authors would like to thank Dr. Jacek Goliński from Institute of Manufacturing Processes, Warsaw University of Technology for preparing samples and Dr. Adam Pietras from Department of Friction and Resistance Welding and Environmental Engineering, Institute of Welding in Gliwice for conducting FSW process.

Abstract

Joints made from ultrafine grained aluminium alloy 1050 are investigated in order to examine the corrosion behavior and microstructural changes between base materials and stir zones. Incremental

ECAP (I-ECAP) was used in order to achieve ultrafine grained structure. Samples in the initial state, after four and eight passes of I-ECAP process were joined with similar plates using Friction Stir Welding (FSW). Initially refined microstructure after I-ECAP transformed to homogenous few micron sized grains structure in stir zones. AlFeSi particles present in the microstructure became fragmented during plastic deformation in I-ECAP. Welding process caused their further fragmentation due to the frictional forces. Despite the significant changes in microstructure the results of electrochemical testing are similar and both I-ECAP processed and FSW samples exhibit comparable corrosion behavior as commercially available 1050-H24 aluminium. The observed minor differences include: slightly higher values of corrosion potentials but more complex pits' morphology for I-ECAP processed samples comparing to the stir zones. The pits in stir zones covered smaller surface area but they exhibit a greater depth. The pits nucleate in the surroundings of the AlFeSi particles. For stir zones, where particles are refined, the number of pits is reduced in comparison to base materials.

1. Introduction

Aluminium and its alloys are widely used in a number of applications because of its excellent corrosion resistance and very good formability of sheets and bars during metal forming. In structural applications, one of the major requirements is high mechanical strength, which can significantly be improved by grain refinement down to submicrometer scale. The yield strength scales with the inverse square root of the grain size (so called Hall-Petch relationship), thus reduction in grain size constitutes one of the most efficient strengthening mechanisms. Ultrafine grained (UFG) materials can be obtained for example employing Severe Plastic Deformation (SPD) processes.[1] Among SPD methods, Equal Channel Angular Pressing (ECAP) represents one, which is currently known as one of the most developed.[2] The material deformation is performed by a simple shear[3], while a sample is pressed through two intersecting channels with the same cross-sections.[4]

ECAP was also a subject of a number of modifications to improve its effectiveness and possibility to process hard-to-deform materials, e.g. additional back pressure[5], rotary die[6], matrix with two parallel channels[7] or with two converging billets[8] to mention only a few of such modifications. Recently, Incremental ECAP (I-ECAP)[9] has been developed and proved as an efficient method of producing UFG metals in the form of plates[10] or bars.[11] In particular, the plate shape seems to be very promising in the case of further applications.

One of the important issues for UFG materials is a lack of reliable joining technologies, which would not destroy UFG structure responsible for high mechanical strength. Friction Stir Welding (FSW)[12] is a promising approach because the process is conducted in a solid state (well below melting point). It brings many advantages, such as absence of porosity, embrittlement or second phase formation. The presence of stable connection is achieved during FSW by mixing the friction-heated, plasticized and deformed metal along the contact line of welded elements. It can be performed by moving a rotating tool (a pin with the shoulder) along the joining line. The key factor for obtaining a consistent joint is a large plastic deformation at elevated temperature. It results in bringing-up atoms to a distance, which allows creation of a metallic bond. Accompanied by increased density of lattice defects, the final microstructure in different joint areas is mainly dependent on dynamic recrystallization and/or recovery.[13] This is especially common for materials such as aluminium, which is characterized by high stacking fault energy. In our previous work[14], we have demonstrated that despite the deterioration of mechanical properties and grain growth in joints compared to hardened base material, good quality butt joints were produced using FSW for UFG aluminium plates. Moreover, the obtained results are promising in comparison to other methods of joining aluminium.

In the present study, we focus on corrosion behavior in aggressive environment as welds or joints are frequently the weak points in the constructions. The microstructure changes caused by the joining processes affect the interactions between material and the environment. The most important factor influencing electrochemical response is surface energy and all areas causing its disorder such

as surface defects (cavities, crevices), grain boundaries, second phase particles or inclusions. In UFG materials, increased number of grain boundaries may influence their electrochemical response in comparison to their coarse grained equivalents. However, the results in the literature are ambiguous. Some studies show that increased number of grain boundaries and dislocations causes a deterioration of the corrosion resistance of aluminium.[15] On the other hand, UFG microstructure can be responsible for easier formation of even more integral passive film[16] in comparison to coarse grained counterparts, which in turn can improve corrosion resistance. Also, particles (in particular primary ones) have a great impact on corrosion behavior. If they act as a cathode, their fragmentation during plastic deformation may result in improved corrosion properties due to the reduction of the cathodic surface.[17]

In this study, the correlation between microstructure changes in base materials (due to SPD processing) and stir zones (due to FSW processing) and their electrochemical response will be discussed with the main emphasis on the influence of grains, grain boundaries and particles.

2. Experimental

The investigated material was commercially pure aluminium (99.50 wt.%). According to EN AW-1050A-H24, the main impurities are Si (max. 0.25 wt.%) and Fe (max. 0.40 wt.%). Material was supplied in the form of 3 mm thick cold rolled sheets. The samples with dimensions of 3 x 62 x 105 mm were processed using I-ECAP[18] to obtain UFG structure. The applied deformation route was based on the rotation of plates about their longitudinal axis by 180˚ between passes (so called route C). The plates were investigated in an initial state (0 passes), after four and eight passes of I-ECAP, which corresponds to true strains of 0, 4.6 and 9.2, respectively. To simplify the sample description, they were described as sample ‘0_BM’, ‘4_BM’ and ‘8_BM’, where BM stands for base material and the number corresponds to number of applied passes. The plates of the same type (i.e. subjected to the same processing path) were joined together using FSW, with the tool shoulder diameter of 17 mm and pin diameter of 5.5 mm. Samples were butt welded along Y plane, which means that joints were made along a longer edge of the rectangular plate. Rotational and linear speeds were different

for materials with different number of I-ECAP passes, which comes from their structural differences and which will not be the subject of the present study. The exact values were as follows: 0_BM – 450 rpm and 224 mm/min, 4_BM – 560 rpm and 355 mm/min, 8_BM – 560 rpm and 224 mm/min.

In the present study both microstructural and corrosion experiments were conducted on the plane coincident with the joining plane, as presented in **Figure 1**. This plane corresponds to plane Z in ECAP process. Base materials (BM) and stir zones (SZ) were investigated separately for each weld.

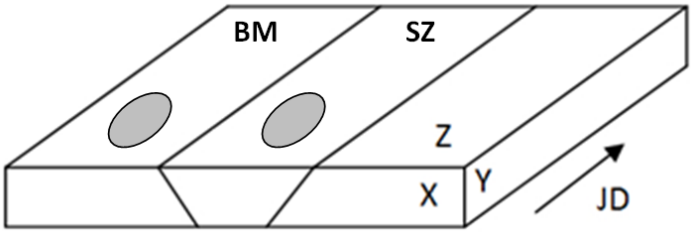

Figure 1. The scheme of samples placement (ellipsoidal patches) used for microstructural and corrosion investigations; JD – joining direction, BM – base material, SZ – stir zone.

Microstructure investigation was conducted using Electron Backscatter Diffraction (EBSD) with analytical Scanning Electron Microscope (SEM) Hitachi SU-70 with acceleration voltage of 20 kV. The samples in the form of thin foils were used. They were prepared using a wire saw, ground down to 150 μm and electropolished using Struers Tenupol-5 system operating at a voltage of 25 V at a temperature of 278K. The EBSD scans were performed separately for the stir zones with a step of 500 nm and base materials with a step of 80 nm. The scanned area contained about 600.000 points in each case. The representative areas have been chosen to present. Grain size was determined by calculating the equivalent diameter, d_2, defined as the diameter of a circle with equal area as the investigated grain, grain size diversity by coefficient of variation *CV(d)* (a ratio of standard deviation to *d*) and grain elongation by a shape factor α defined as a ratio of maximum diameter of a grain to its equivalent diameter, d_{max}/d_2. The measurements included both grains and subgrains. The fraction of high angle grain boundaries (HAGBs) having misorientation angle γ higher that 15˚ was

also determined. SEM observations were also used in order to characterize the particles observed in the microstructure. Samples were prepared the same way as for EBSD investigation.

Before each electrochemical test, the samples were mechanically ground up to 4000 SiC grit paper and then ultrasonically degreased in ethanol. Electrochemical experiments were carried out in 3.5% NaCl using the AutoLab PGSTAT32N potentiostat/galvanostat. The measurements were repeated in triplicate at a minimum on each sample. The conventional three-electrode cell was used with a Pt wire as the counter electrode and a silver chloride electrode as the reference one. The ratio of surface area of working electrode to counter electrode was 1:2.5. Potentiodynamic polarization scans were initiated after 30 min immersion at the free corrosion potential at a scan rate of 1 mV/s starting from -300 mV below the open circuit potential until a current density of 10 mA/cm^2 was reached. Corrosion potential (E_{corr}) and corrosion current density (i_{corr}) were evaluated by Tafel extrapolation. Additionally, the current density at cathodic and anodic range at specific potentials (-0.95 $V_{Ag/AgCl}$ and -0.73 $V_{Ag/AgCl}$, respectively) and pitting potential (E_{pit}) were determined from potentiodynamic curves. After potentiodynamic polarization the surfaces of the samples were investigated using SEM. The obtained pits were quantitatively analyzed using two parameters: the surface fraction A_A (%), which allows estimating the surface covered by the pits in relation to the whole surface and the number of pits per unit surface N_A ($1/\mu m^2$). Pits with area above 1 μm^2 were considered.

3. Results

3.1. Microstructure

In order to characterize the grain structure and grain boundaries, EBSD measurements were conducted. Orientation imaging maps (OIM) for the base materials and stir zones are presented in Figure 2. High Angle Grain Boundaries (HAGBs, $\gamma \geq 15^{\circ}$) are highlighted in black, while Low Angle Grain Boundaries (LAGBs, $3^{\circ} \leq \gamma < 15^{\circ}$), which are less distinct, in grey. The quantitative

data regarding the grains sizes, shapes, grain size diversity and fraction of HAGBs is summarized in Table 1.

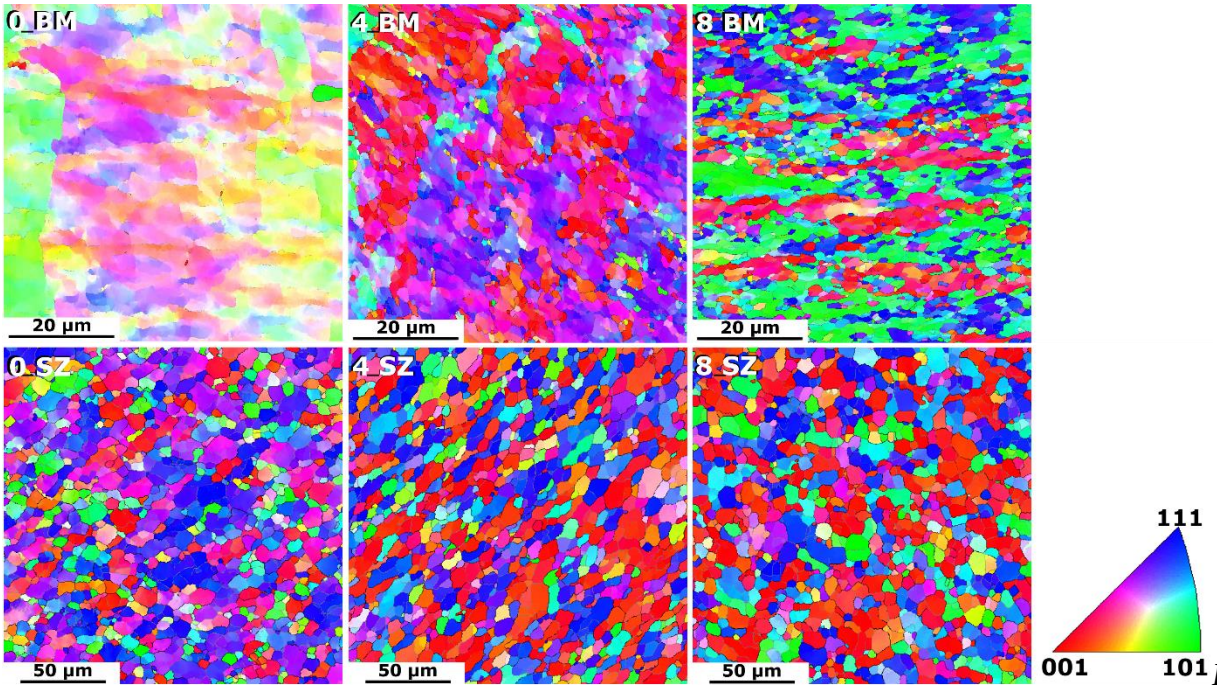

Fig. 2. Orientation maps for base materials (BM) stir zones (SZ); the number indicates the number of I-ECAP passes.

The 0_BM sample features elongated grains with a great majority of LAGBs. Only 2.9% of boundaries are of high angle type. As a result, orientation map with no distinct boundaries can be seen. The average grain/subgrain size d_2 is less than 3 µm, but the grain size distribution is very wide, as quantified by the very high value of CV(d) parameter – 4.59. Processing up to four I-ECAP passes (4_BM sample) resulted in a considerable grain size reduction (d_2) down to 1.28 µm and elevated fraction of HAGBs (40.5 %). The grain sizes are much more uniform, as evidenced by the CV(d) value which equals 1.32. The shape factor α is comparable to that for the initial state and equals 1.46 suggesting fairly equiaxial microstructure. Further processing, up to eight I-ECAP passes (8_BM sample), caused further increase in orientation diversity. As a result, the amount of HAGBs increased up to 53.1 %. The average grain size decreased to d_2=1.16 µm. Grain size distribution is significantly reduced, indicating more uniform grain size distribution. However, the grain shape factor is slightly higher than for 4_BM sample.

The microstructure in stir zones is quite different. As it can be seen that the grain growth occurred in the stir zone for each sample. The average grain size ranges from d_2=5.91 to d_2=6.25 μm for 0_SZ and 8_SZ samples, respectively. The coefficient of variation is in the range of 0.62-0.69, revealing very low diversity in grain sizes. Shape factor α indicates grains with shape close to equiaxial. The fraction of HAGBs is higher than 60% for all the SZ samples.

Table 1. Microstructural parameters: average grain size, d_2, grain size distribution, CV(d), shape factor, α, and the fraction of HAGBs for BMs and SZs.

	0_BM	4_BM	8_BM	0_SZ	4_SZ	8_SZ
d_2 [μm]	2.79	1.28	1.16	5.91	6.2	6.25
CV (d)	4.59	1.32	0.79	0.69	0.62	0.62
α	1.43	1.46	1.51	1.41	1.48	1.39
HAGB [%]	2.9	40.5	53.1	62.3	68.1	65.3

The SEM images of base materials and stir zones are presented in Figure 3 to illustrate changes in the morphology, size and distribution of primary intermetallic particles. They are visible as white particles (they could not be recognized in EBSD) and were identified as AlFeSi phase by EDS analysis. Other typical inclusions for aluminium 1050, such as Al_2O_3 or MgO[19] were not found. The stereological parameters describing AlFeSi particles, the same as for the grains, are summarized in Table 2. It should be noted that in the measurements of particle size, the clusters of particles were assumed as one particle. The average size of particles d_{2p} in 0_BM sample is about 1 μm and it decreases with increasing number of I-ECAP passes, down to 470 nm for 8_BM sample. In addition, the values of both coefficient of variation CV_p (d) and shape factor α_p decrease too. It indicates that plastic deformation caused the fragmentation of particles and their clusters. The clusters with the sizes of even several tens of micrometers are mainly observed in 0_BM sample.

Along with the progressive plastic deformation, the number and size of such clusters is getting lower, but they are still present in the microstructure. Nevertheless, the values of stereological parameters are decreasing with increasing I-ECAP passes, leading to more equiaxial shape and smaller sizes of particles.

The particles of stir zones as visible in SEM are presented in Figure 3, with two magnifications. It should be noted that the AlFeSi particles have changed their size and shape. The particles are divided into smaller pieces due to frictional forces. No more clusters of particles can be observed. The average particle size decreased down to 380, 250 and 130 nm for 0_SZ, 4_SZ and 8_SZ samples, respectively. With increasing number of I-ECAP passes, the average particle size is reduced. The AlFeSi particles are not only smaller but also much more equiaxial in shape and their size distributions are much more uniform, as very low values of elongation factor (1.15 – 1.18) and coefficient of variation (0.06 – 0.14) were obtained, as presented in Table 2. Particles are observed in both – grain boundaries and grain interiors, without any preferences.

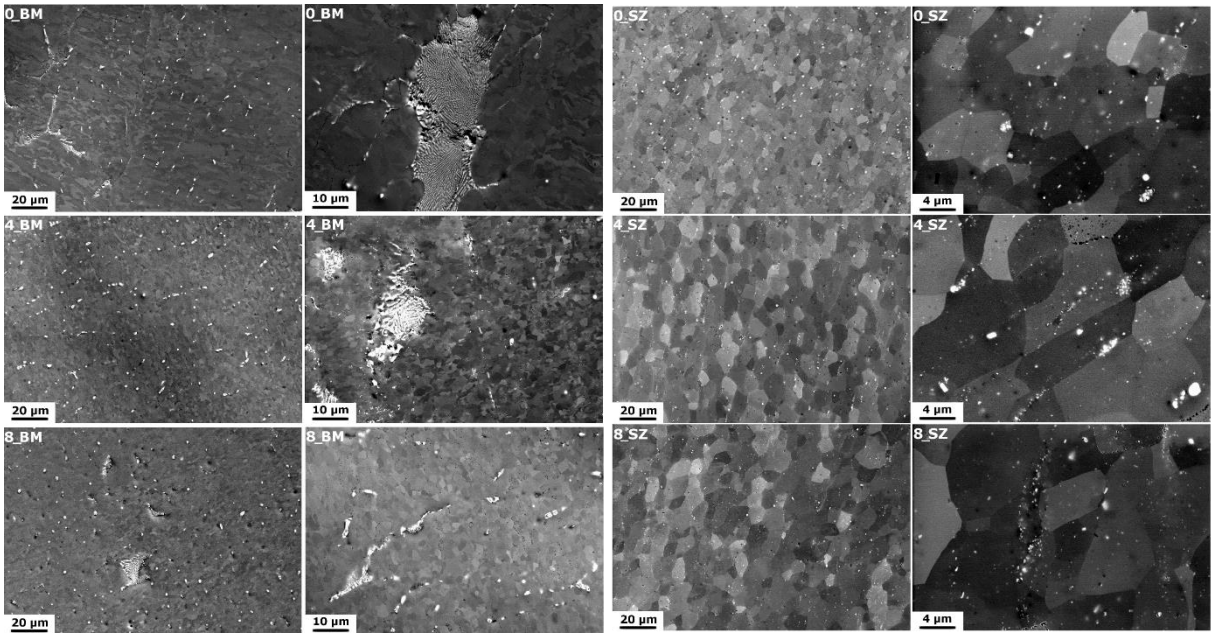

Figure 3. Microstructure of base materials (BM): in an initial state (cold rolled plate – 0_BM) and after different stages of I-ECAP processing (4_BM & 8_BM) and of stir zones

Table 2. Stereological parameters describing AlFeSi particles present in the microstructure of base materials (BM) and stir zones (SZ). The number indicates the number of I-ECAP passes.

	0_BM	4_BM	8_BM	0_SZ	4_SZ	8_SZ
d_{2p}[μm]	0.93	0.64	0.47	0.38	0.25	0.13
CV_p (d)	0.40	0.38	0.30	0.14	0.10	0.06
α_p	1.43	1.28	1.27	1.18	1.15	1.15

3.2. Resistance to pitting corrosion

The representative potentiodynamic polarization curves after 30 min of immersion in the test solution are shown in Figure 4. The electrochemical parameters obtained from the curves are listed in Table 3.

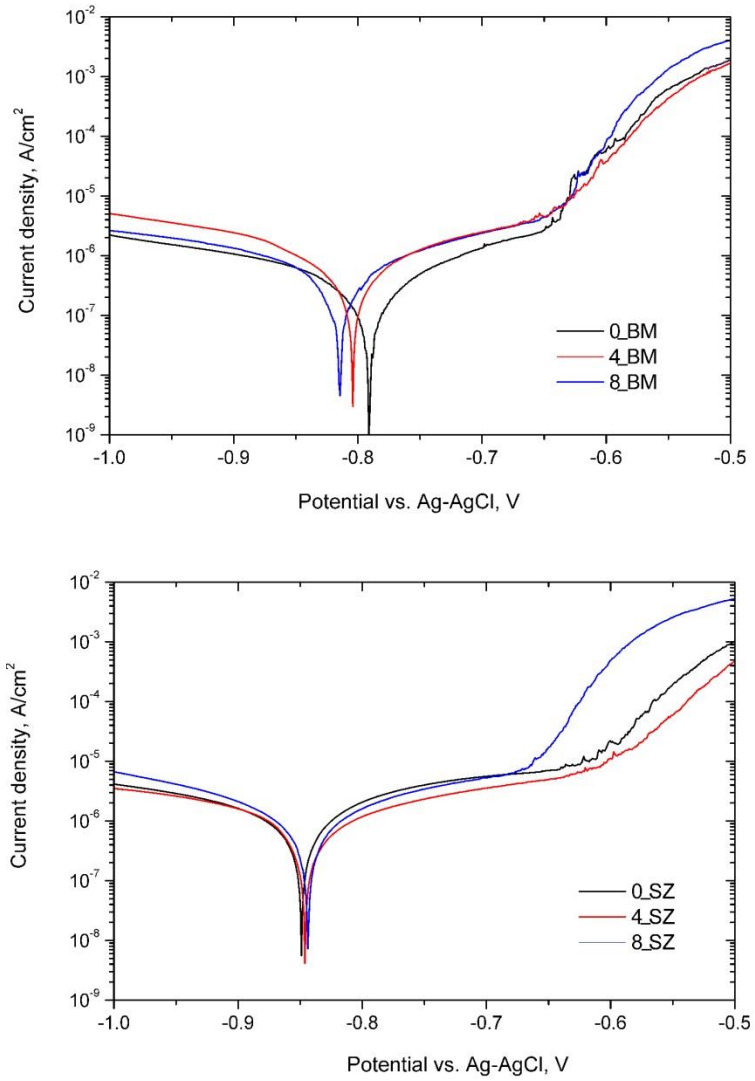

Figure 4. Electrochemical testing for BM (upper diagram) and SZ (lower diagram) samples - potentiodynamic polarization curves recorded in aerated 3.5% NaCl at room temperature.

For the BM samples, the corrosion potential is very similar and slightly decreases with the number of I-ECAP passes (~20 mV) while corrosion current increased about 2 times after processing. Comparing to the SZ samples, the corrosion potentials of BM samples are nobler by about 50 mV and the corrosion current density is lower. The differences in corrosion potentials between the SZ samples are minor. In the cathodic range, the lowest current density was observed for 0_BM sample while for 4_BM sample, the cathodic current density was more than two times higher. The highest value of current density in the cathodic range was observed for 8_SZ sample. The current density in

the passive range was the lowest for 0_BM sample and after the I-ECAP process it increased nearly two times. For SZ samples, the current density in the passive range decreased after the I-ECAP process but it was still higher comparing to BM samples. For all tested samples, the pitting potential (E_{pit}) was in the range from -0.67 V up to -0.61 V. It indicates that the I-ECAP process has nearly no impact on the breakdown potential of BM samples. The susceptibility to localized attack is lower for the 0_SZ and 4_SZ samples than for BM samples, and is slightly higher for 8_SZ sample.

Table 3. Corrosion potential (E_{corr}), corrosion current density (i_{corr}), pitting potential (E_{pit}), current density at cathodic and anodic range at specific potentials (i_{cath} at -0.95 $V_{Ag/AgCl}$ and - i_{pass} at 0.73 $V_{Ag/AgCl}$); the surface fraction A_A and the number of pits per unit surface N_A.

Sample	E_{corr} [$V_{Ag/AgCl}$]	i_{corr} [$\mu A/cm^2$]	i_{cath} at -0.95 $V_{Ag/AgCl}$, [$\mu A/cm^2$]	i_{pass} at -0.73 $V_{Ag/AgCl}$, [$\mu A/cm^2$]	E_{pit}, [$V_{Ag/AgCl}$]	N_A, [$1/\mu m^2$]	A_A, [%]
0_BM	-0.78	0.5	1.5	0.9	-0.64	$1.2*10^{-3}$	1.84
4_BM	-0.80	1.1	3.7	1.7	-0.65	$2.2*10^{-3}$	3.32
8_BM	-0.81	1.0	2.0	1.7	-0.65	$2.2*10^{-3}$	3.61
0_SZ	-0.84	2.1	2.8	4.5	-0.61	$6.3*10^{-4}$	1.65
4_SZ	-0.85	1.5	2.5	3.0	-0.61	$3.0*10^{-4}$	1.66
8_SZ	-0.84	1.6	3.9	3.9	-0.67	$4.3*10^{-4}$	1.29

The post-corrosion surface morphology was examined using SEM in SE mode. Figure 5 illustrates the surface for the BM and SZ samples. There are some differences in the morphology of the corrosion attack between the BM and SZ samples. The quantitative results of analyzed pits are presented in Table 3. In the base materials, pits have more developed morphology. Pits in BM

samples, especially after I-ECAP, are irregular in their shape. From the initial pits, many branches are coming, creating the network of shallower pits. Only 0_BM sample exhibits less developed pits, similar to the SZ samples. The area occupied by pits increases with I-ECAP processing, as can be seen from increasing value of parameter A_A. With increasing number of passes, the branches are more frequent and cavities are longer. In SZ samples, the pits are much more regular. The branches are also present, but their length is significantly reduced in comparison to BM samples. All SZ samples are characterized by the similar pits morphology. They cover a significant smaller area than pits in BM, as the A_A parameter is much more reduced. Nevertheless, the depth of pits in SZ is bigger than in base materials. The number of pits per unit area (N_A) is smaller than in base materials, but it should be noted, that only pits of area higher than 1 μm^2 were taken into consideration. In all samples, the pits morphology has crystallographic nature, as their planes are similar to crystallographic planes. Such a character of pits was observed in different aluminium alloys also with many linked cavities.[20] In our case, the same corrosion attack is observed, with each pit as a network of crystallographically-faceted cavities The facets are likely to be {100} planes. Moreover, it can be assumed that the crevice between the particle and the matrix can act as a pit nucleation site.

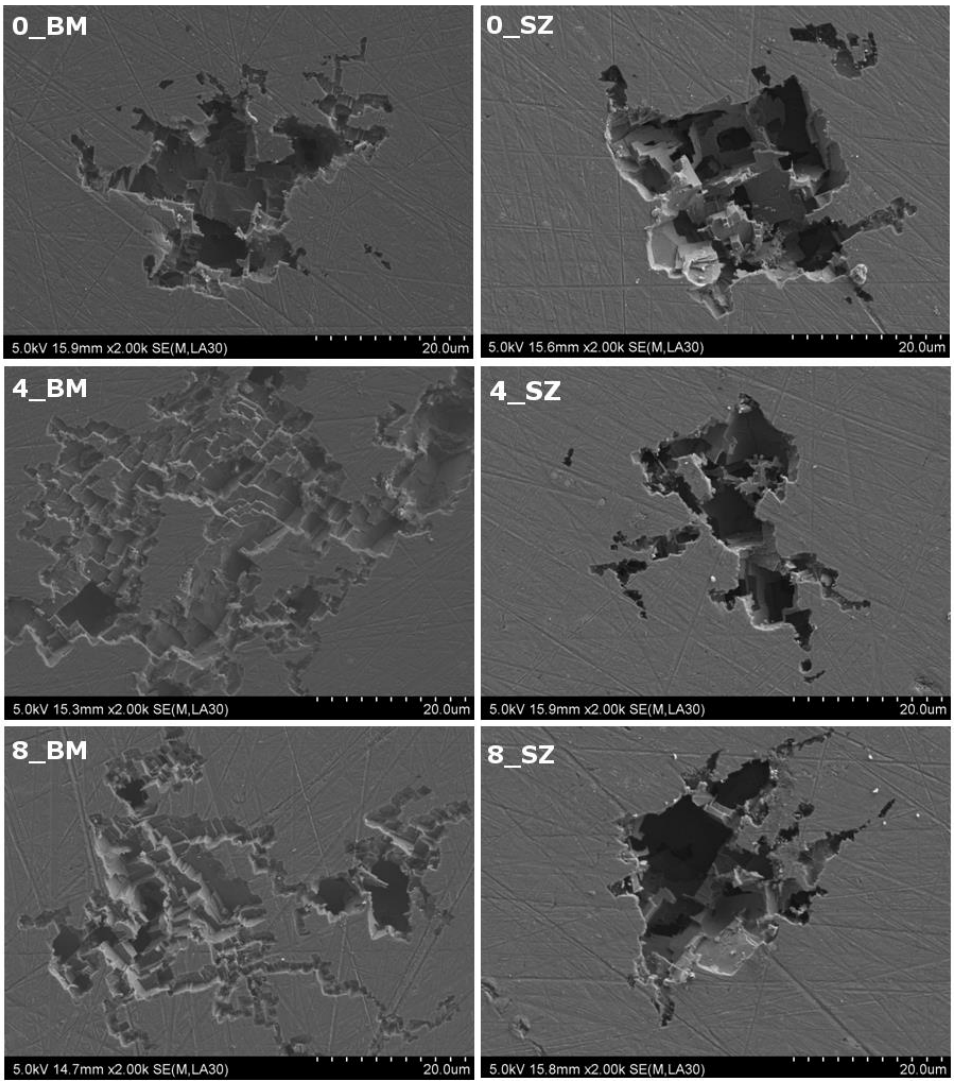

Figure 5. Morphology of corrosion attack after potentiodynamic tests of base materials (BM) and stir zones (SZ); the number indicates the number of I-ECAP passes of the initial material.

4. Discussion

4.1. I-ECAP deformation route C

The deformation route C (with rotation about X axis by 180^{o} between every pass), selected in the present study, has a great technological advantage, i.e. it allows to process very long flat products. In the present study, the length of the billet was only twice higher than the width but it can be increased very easily by using feeding the billet during I-ECAP[21] instead of pushing it[9] into

shearing zone. Figure 6 shows a relationship between position of shearing planes SP and shearing directions SD in two consecutive ECAP passes performed with route C. In route C, the shearing occurs on two crossing planes in each subsequent pass, but the shear direction is reversed in each pass. It is known as not the most optimal route in terms of grain refinement and the formation of HAGBs.[22] Four I-ECAP passes allowed producing microstructure, which consists of both – ultrafine and micron grains, with HAGBs fraction equals 40.5 % (see Table 1). Deformation up to 8 passes caused further slight grain refinement (from 1.28 and 1.16 μm), however, some fraction of elongated grains with subgrains inside is still present in the microstructure. It also resulted in the increase of misorientation angles of grain boundaries. The amount of HAGBs increased up to 53.1%. These results are comparable to route C applied in traditional ECAP process, where elongated grains remained in microstructure even under high strains.[23] In comparison, the I-ECAP processing with the rotation about Z axis by 90° between every pass[24] brought about uniform equiaxial grains with the size of about 600 nm and the content of HAGBs reaching 80%. This means that the microstructure, although typical for ECAP route C, is not fully transformed into equiaxial UFG one, which may be a reason of minor differences in corrosion behavior of BM samples.

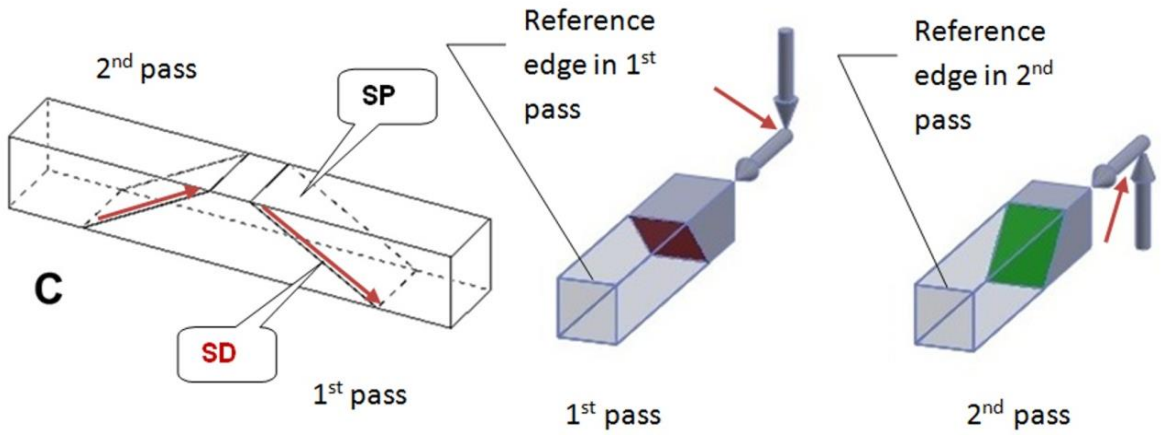

Figure 6. Positions of shear planes SP and shear directions SD in two consecutive ECAP passes in route C and their explanation.

4.2. Microstructure transformation in stir zone

Friction stir welding of coarse grained materials leads to grain refinement in SZ due to the dynamic recrystallization during plastic deformation and heating caused by the friction between the welding tool and the workpiece.[25] It results in the presence of few microns sized grains in stir zone. In the case of UFG materials, where internal energy is enhanced, further grain refinement cannot be achieved. Contrary, grain growth is observed because the temperature rise during FSW is high enough to induce recrystallization.

Literature data shows that samples after SPD processing, especially pure metals, are prone to grain growth during FSW. For example, the samples after Accumulative Roll Bonding (ARB)[26] underwent the grain growth from 0.6 μm to even 3.2 μm. It should also be noted that comparable grain sizes in the stir zone were observed for joints made from as-received samples and after ARB, which differed significantly in grain sizes. For the initial state the average grain size equaled about 13 μm, after ARB as above - 0.6 μm. On the other hand, for samples subjected to Constrained Groove Pressing (CGP)[27], the microstructure and mechanical properties of stir zones differed for one and two passes. With higher applied strain, grain growth was observed due to the temperature rise during FSW. Nonetheless, for smaller strain (one pass of CGP) the average grain size in stir zone decreased and even the increase in microhardness was noticed. The explanation may lie in the partial restoration phenomenon, which compensates the dislocation density reduction, leading to increase in grain boundaries density at a specific temperature range.[28]

In the present study the initial state, which was cold rolled plate, had initially about 3 μm grain size and a very high fraction of LAGBs. The stir zone of this sample reveals the lowest value of the average grain size. As can be seen, the differences in applied strain between four and eight passes were not sufficient to reveal distinct differences between these two states. Nonetheless, grain growth in these samples is higher than for the cold rolled plate. The reason lies in thermal stability, which is lower for materials with UFG microstructure than their coarse grained counterparts. In

aluminium alloy 2xxx during 1h annealing the ultrafine grained structure is stable up to 200˚C. Annealing at 400˚C caused abnormal grain growth from 100 nm after deformation up to 12 μm. Pure aluminium with UFG structure is even more unstable and the extensive grain growth occurs during annealing above 200˚C.[28] The peak temperature during FSW is in the range from 0.6 to even 0.95 T_{melt}, and depends on the material, tool arrangement and process conditions.[13] The temperature was not measured in present study. Nevertheless, even in the lower limit this peak is high enough to completely reorganize the microstructure in stir zone. With the higher internal stresses after SPD processing, the microstructure is more unstable, which results in faster grain growth. Therefore, the grain growth is the most distinct in sample after eight passes of I-ECAP and the least – for cold rolled plate.

4.3. Intermetallic particles

The last issue concerning the microstructure, which needs to be discussed, is the evolution of AlFeSi particles. They are present in base materials in the form of both clusters and as separate platelets. For cold rolled plate (0_BM sample) the largest concentrations of particle clusters can be seen. I-ECAP processing caused particles fragmentation. With increasing number of passes the average particle size decreased from 0.93 μm to 0.47 μm. Such phenomenon has been observed previously for SPD processing. For 2xxx alloy after hydrostatic extrusion the size of even small particles decreased and their distribution became more homogenous.[29] Also inclusions containing Si in aluminium alloy 1050 have been fragmented and more uniformly distributed during processing via ECAP.[17] In casted Al-7%Si alloy the Si particles size decreased from 4 to 1.4 μm after ten ECAP passes.[30] With the increased content of Si up to 10%, the fragmentation of Si particles can be even more pronounced, from 19 μm for the as-cast condition to 0.8 μm after ECAP processing.[31] I-ECAP processing also affected the shape and concentrations of particles as shown in the present study. With further processing their distribution became more uniform. The presence

of particles located in clusters is still observed. Nevertheless, their size is reduced in comparison to the initial state.

In stir zone, there is an evidence for particle size reduction and their distribution became closer to uniform. The average particle size decreased significantly during FSW process. There are no more clusters of AlFeSi particles. The average size of particles size is decreasing from 380 to 130 nm, with increasing number of I-ECAP passes for the stir zone. Particles fragmentation during FSW is rather common phenomenon. It was observed in 6082 aluminium alloy after FSW, that intermetallic particles were severely deformed and sheared.[32] This phenomenon was also observed in 2xxx alloys[33], where Fe-containing particles were fragmented due to the stirring during FSW process. Nevertheless, at the same time a coarsening of S-precipitates was also observed due to the temperature rise during FSW. In the investigated pure aluminium, only fragmentation of primary particles is observed, as precipitates are not present.

4.4. Electrochemical behavior

The results obtained in the present study clearly demonstrate that despite the changes in the microstructure (i.e. grain refinement, fragmentation of intermetallic particles) due to both I-ECAP processing and FSW, the corrosion behavior is only slightly affected and UFG materials as well as FSW joints exhibit the corrosion resistance comparable to commercially available 1050-H24 aluminium. It should be noted that literature data regarding electrochemical behavior of UFG materials are ambiguous and show that the corrosion resistance of aluminium and its alloys can be either enhanced or deteriorated by the SPD processes. In the case of Al-Ni and Al-Cu alloy processed by ECAP[15] or Al-Si after HPT[34], the applied processes caused the increase in corrosion resistance. Such a behavior was attributed to the presence of second phase particles and changes in their size, shape and distribution after plastic deformation. For pure aluminium, the corrosion resistance after ECAP was reduced.[15] Completely different results were obtained for pure aluminium after rotary swaging, where the grain refinement caused higher corrosion resistance in

comparison to coarse grained materials.[16] This phenomenon was explained by the easier formation of passive films due to the elevated amount of defects such as grain boundaries and dislocations, where oxidation of metal occurs. Furthermore, internal stresses present in UFG structure were connected to stable and integral passive film. It was also reported[17] that the corrosion resistance increased with the increasing number of ECAP passes for aluminium alloy 1050. Si-containing impurities after ECAP processing became smaller and more homogenously distributed. The smaller area of impurities, which behave as a cathode, the greater pitting resistance, as a cathode area was reduced.

The AlFeSi particles present in the investigated microstructures act as cathodes while the Al-matrix as an anode, as it can be seen in Figure 7. The pits initiate mostly in the vicinity of AlFeSi particles, where the area next to the particles has been degraded. Since I-ECAP processing causes the particles fragmentation, it can be expected that the corrosion resistance will be enhanced. However, I-ECAP processing led to a reduction in the corrosion potential. Nonetheless, the differences in the range of 10-20 mV are rather low. Similarly, the pitting potential is lowered for deformed samples, but only by 10 mV. The achieved differences are insignificant. However, BM samples differ in pits morphology. As it was shown, for all the samples crystallographic pits are observed, which consist of crystallographically-faceted cavities. It is common for aluminium and its alloys that in aggressive environment, the dissolution is performed in planes similar to {100}.[20] With increasing number of I-ECAP passes, the cavities are becoming larger and more numerous. As a result larger area is covered in pits. For samples after SPD processing the cavities can achieve even tens of microns. The length of them is connected with the grain size, because as was shown, the smaller average grain size the greater length of such cavities. The type of grain boundaries can stimulate the process of cavities propagation, therefore further investigation needs to be perform, in order to clarify the

process of pits growth.

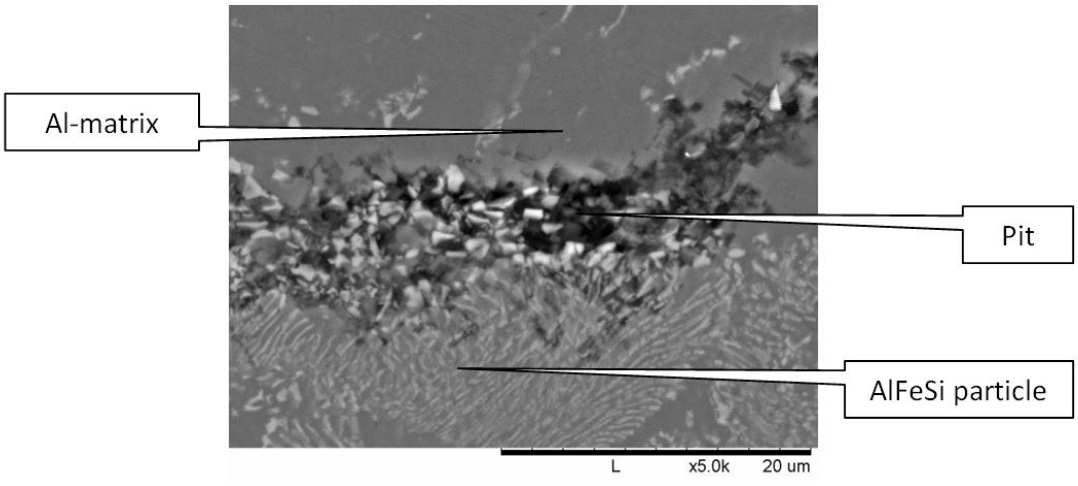

Figure 7. Initiation of pits in the surroundings of AlFeSi particles.

The SZ samples reveal lower values of corrosion potential, which may indicate a lower resistance to corrosion attacks than BM samples. Nevertheless, the number of pits is lower than in BM samples. The morphology of pits for SZ samples differs from those obtained for base materials. The pits are less developed. Only a few cavities coming from the initial pits can be observed. Therefore, the pits area is reduced in comparison to BM samples, which can be seen from reduced values of A_A parameter. Hence, the total area touched by the corrosion attack is smaller than in base materials, where pits are more widespread because of the cavities. On the other hand, the pits in stir zones are deeper and therefore more dangerous in terms of future potential applications in harsh environment. The differences in the microstructure between these two zones consist of different grains and particles sizes. The conclusion can be drawn, that the smaller average grain size the more diverse pit's morphology with more developed cavities but with smaller depth. Samples from base materials, where AlFeSi particles were bigger, reveal higher number of pits. The second conclusion can be drawn, that the size of particles play a role in pits initiations. The critical size of particles has to be achieved to initiate the pit's growth. Therefore, the number of pits in SZ samples is smaller, despite the larger number of particles. It is evidently seen in 8_SZ sample, where a large number of

particles is seen, but their size is so small, that only small percentage of them caused the pits initiation, as can be seen form the number of pits (Table 3).

The observed differences in pits morphology between areas with different grain sizes are in contrary to results obtained in[35], where for UFG samples of Al-Mg alloys the pitting corrosion was strongly localized and pits penetrated in depth. In the present study, samples with UFG microstructure reveal shallow pits but with greater surface areas. Contrary, stir zones, where coarse grained structure was achieved, revealed higher depth of pits. Nevertheless, the behavior of corrosion attack can be different for different materials with varying grain sizes. As was presented for AA2024, the grain refinement can cause even the change in corrosion attack from intergranular to pitting, resulting in a relative reduction in attack depth.[36]

FSW process has been chosen because joints produced from aluminium alloys by this method reveal better electrochemical properties than joints obtained by other arc welding processes, such as Metal Insert Gas.[37] The stable connection and lack of harmful defects cause FSW joints of very high corrosion resistance. As it was demonstrated, corrosion resistance of FSW materials depends on several process parameters, such as travelling speed[38] or tool geometry.[39] However, there are some inconsistencies regarding the corrosion resistance of joints compared to the initial states of material to be joint materials. In[39], the enhancement of corrosion resistance of aluminium alloy AA2219 in stir zone has been achieved and it was attributed to the dissolution of precipitates in this zone. Contrary, in[40] the lower corrosion resistance in the weld zone of aluminium alloy AA6061 was obtained in comparison to the base material. These differences are caused by the microstructure and chemical composition of the base material. The present study revealed slight differences between the base materials and joints. The electrochemical parameters do not vary significantly, but there is a difference in pits number and morphology between these two areas. Stir zones reveal lower number of pits, which cover additionally lower area, but they pose greater depth, which can be assumed as more dangerous in terms of potential applications.

5. Conclusions

1. Both I-ECAP and FSW processes induce significant changes in the microstructure of AA1050:
    a. I-ECAP results in a grain refinement from 2.79 μm to 1.16 μm and an increase in the fraction of HAGBs from 2.9 % up to 53.1%, as measured for plane Z;
    b. FSW process causes a grain growth in the stir zones - the average grain size increased to about 6 μm.
    c. AlFeSi particles present in the microstructure have been fragmented during I-ECAP and FSW processes: primary clusters of large particles have been transformed into smaller and separated particles after I-ECAP while FSW process led to further significant particles fragmentation and caused their uniform distribution.
2. I-ECAP processing has a minor influence on the electrochemical response of 1050 aluminium. The changes of pit morphology can be seen, as with increasing number of I-ECAP passes the pits exhibit more complex structure with linked cavities.
3. Stir zones reveal only slightly lower corrosion potential than the base materials. Pits in stir zones are less developed, with only few cavities, but their depth is much higher than the depth of pits in base materials. Both the number and area covered by pits is lower than for base materials.
4. Finally, it can be concluded that UFG samples as well as FSW joints exhibit the corrosion resistance comparable to commercially available 1050-H24 aluminium.

Received: ((will be filled in by the editorial staff))
Revised: ((will be filled in by the editorial staff))
Published online: ((will be filled in by the editorial staff))

[1] T.G. Langdon, Acta Mater. **2013**, *61*, 7035–7059.

[2] R.Z. Valiev, T.G. Langdon, Prog. Mater. Sci. **2006**, *51*, 881–981.

[3] V.M. Segal, Mater. Sci. Eng. A. **1995**, *197*, 157–164.

[4] M. Furukawa, Y. Iwahashi, Z. Horita, M. Nemoto, T.G. Langdon, Mater. Sci. Eng. A. **1998**, *257*, 328–332.

[5] P.W.J. Mckenzie, R. Lapovok, Acta Mater. **2010**, *58*, 3198–3211.

[6] A. Ma, Y. Nishida, K. Suzuki, I. Shigematsu, N. Saito, Scr. Mater. **2005**, *52*, 433–437.

[7] Z.Y. Liu, G.X. Liang, E.D. Wang, Z.R. Wang, Mater. Sci. Eng. A. **1998**, *242*, 137–140.

[8] A. Rosochowski, L. Olejnik, J. Richert, M. Rosochowska, M. Richert, Mater. Sci. Eng. A. **2013**, *560*, 358–364.

[9] L. Olejnik, W. Chrominski, a Rosochowski, M. Lipinska, M. Lewandowska, IOP Conf. Ser. Mater. Sci. Eng. **2014**, *63*, 012004.

[10] L. Olejnik, A. Rosochowski, M. Richert, Mater. Sci. Forum. **2008**, *584-586*, 108–113.

[11] A. Rosochowski, L. Olejnik, M. Richert, Mater. Sci. Forum. **2008**, *584-586*, 139–144.

[12] B.T. Gibson, D.H. Lammlein, T.J. Prater, W.R. Longhurst, C.D. Cox, M.C. Ballun, et al., J. Manuf. Process. **2014**, *16*, 56–73.

[13] T.R. McNelley, S. Swaminathan, J.Q. Su, Scr. Mater. **2008**, *58*, 349–354.

[14] M. Lipińska, L. Olejnik, A. Pietras, A. Rosochowski, P. Bazarnik, J. Goliński, et al., Mater. Des. **2015**, *88*, 22–31.

[15] E. Akiyama, Z. Zhang, Y. Watanabe, K. Tsuzaki, J. Solid State Electrochem. **2009**, *13*, 277–282.

[16] M. Abdulstaar, M. Mhaede, L. Wagner, M. Wollmann, Mater. Des. **2014**, *57*, 325–329.

[17] M.-K. Chung, Y.-S. Choi, J.-G. Kim, Y.-M. Kim, J.-C. Lee, Mater. Sci. Eng. A. **2004**, *366*, 282–291.

[18] M. Lewandowska, W. Chrominski, M. Lipinska, L. Olejnik, A. Rosochowski, Key Eng.

Mater. **2016**, *710*, 59–64.

[19] X. Li, Y. Cao, L. He, Y. Guo, J. Cui, Steel Res. Int. **2013**, *84*, 1223–1229.

[20] R. Ambat, A.J. Davenport, G.M. Scamans, A. Afseth, Corros. Sci. **2006**, *48*, 3455–3471.

[21] A. Rosochowski, L. Olejnik, IOP Conf. Ser. Mater. Sci. Eng. **2014**, *63*.

[22] Y. Iwahashi, Z. Horita, M. Nemoto, T.G. Langdon, Acta Mater. **1998**, *46*, 3317–3331.

[23] T.G. Langdon, Mater. Sci. Eng. A. **2007**, *462*, 3–11.

[24] W. Chrominski, L. Olejnik, A. Rosochowski, M. Lewandowska, Mater. Sci. Eng. A. **2015**, *636*, 172–180.

[25] R.K.R. Singh, C. Sharma, D.K. Dwivedi, N.K. Mehta, P. Kumar, Mater. Des. **2011**, *32*, 682–687.

[26] Y. Sun, H. Fujii, Y. Takada, N. Tsuji, K. Nakata, K. Nogi, Mater. Sci. Eng. A. **2009**, *527*, 317–321.

[27] M. Sarkari Khorrami, M. Kazeminezhad, A.H. Kokabi, Mater. Des. **2012**, *40*, 364–372.

[28] F. Khodabakhshi, M. Kazeminezhad, Mater. Sci. Eng. A. **2011**, *528*, 5212–5218.

[29] M. Lewandowska, K.J. Kurzydłowski, Mater. Charact. **2005**, *55*, 395–401.

[30] I. Gutierrez-Urrutia, M.A. Muñoz-Morris, D.G. Morris, Acta Mater. **2007**, *55*, 1319–1330.

[31] K. Regina Cardoso, M.A. Muñoz-Morris, K. Valdés León, D.G. Morris, Mater. Sci. Eng. A. **2013**, *587*, 387–396.

[32] M. Cabibbo, A. Forcellese, M. El Mehtedi, M. Simoncini, Mater. Sci. Eng. A. **2014**, *590*, 209–217.

[33] M. Jariyaboon, A.J. Davenport, R. Ambat, B.J. Connolly, S.W. Williams, D.A. Price, Corros. Sci. **2007**, *49*, 877–909.

[34] X. Wang, M. Nie, C.T. Wang, S.C. Wang, N. Gao, Mater. Des. **2015**, *83*, 193–202.

[35] J.G. Brunner, J. May, H.W. Höppel, M.Göken, S. Virtanen, Electrochim. Acta. **2010**, *55*, 1966–1970.

[36] J.G. Brunner, N. Birbilis, K.D. Ralston, S. Virtanen, Corros. Sci. **2012**, *57*, 209–214.

[37] S. Maggiolino, C. Schmid, J. Mater. Process. Technol. **2008**, *197*, 237–240.

[38] N.D. Nam, L.T. Dai, M. Mathesh, M.Z. Bian, V.T.H. Thu, Mater. Chem. Phys. **2016**, *173*, 7–11.

[39] C. Venkata Rao, G. Madhusudhan Reddy, K. Srinivasa Rao, Def. Technol. **2015**, *11*, 197–208.

[40] F. Gharavi, K.A. Matori, R. Yunus, N.K. Othman, F. Fadaeifard, J. Mater. Res. Technol. **2015**, *4*, 314–322.

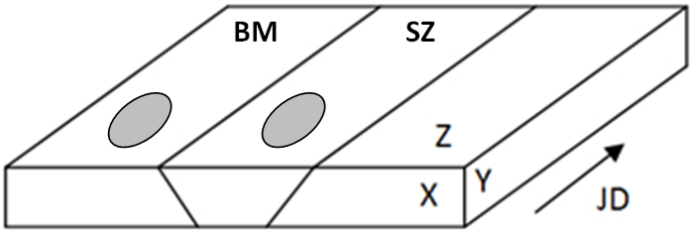

Figure 1. The scheme of samples placement (ellipsoidal patches) used for microstructural and corrosion investigations; JD – joining direction, BM – base material, SZ – stir zone.

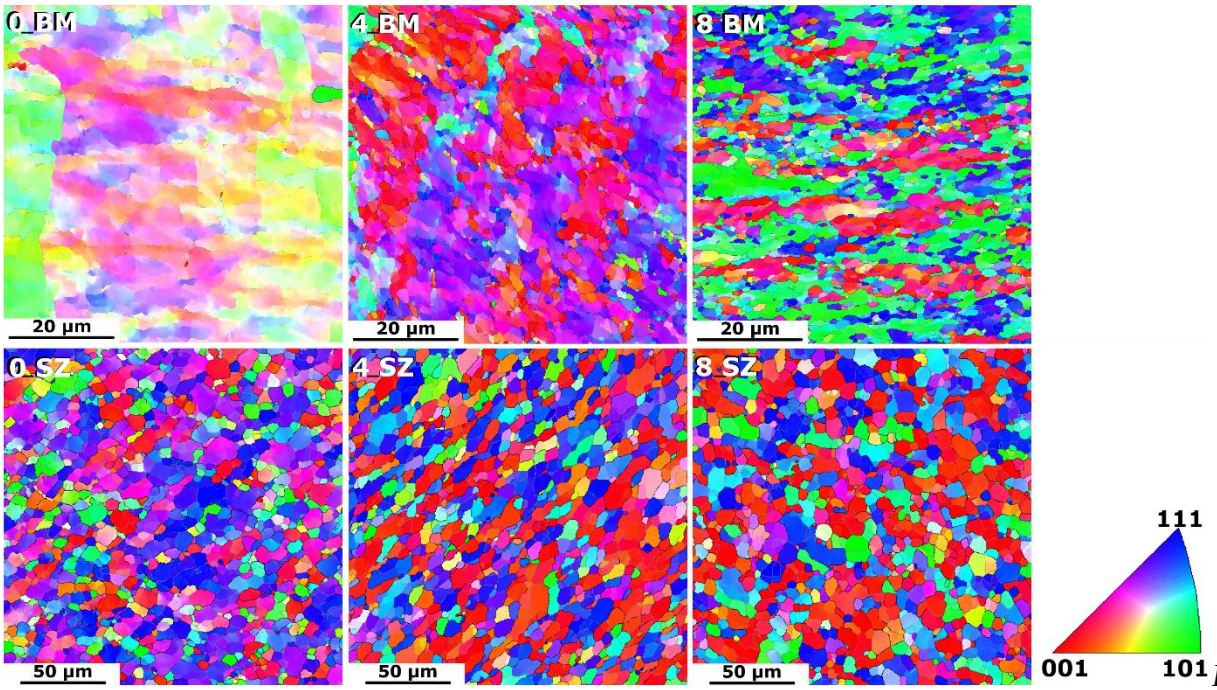

Fig. 2. Orientation maps for base materials (BM) stir zones (SZ); the number indicates the number of I-ECAP passes.

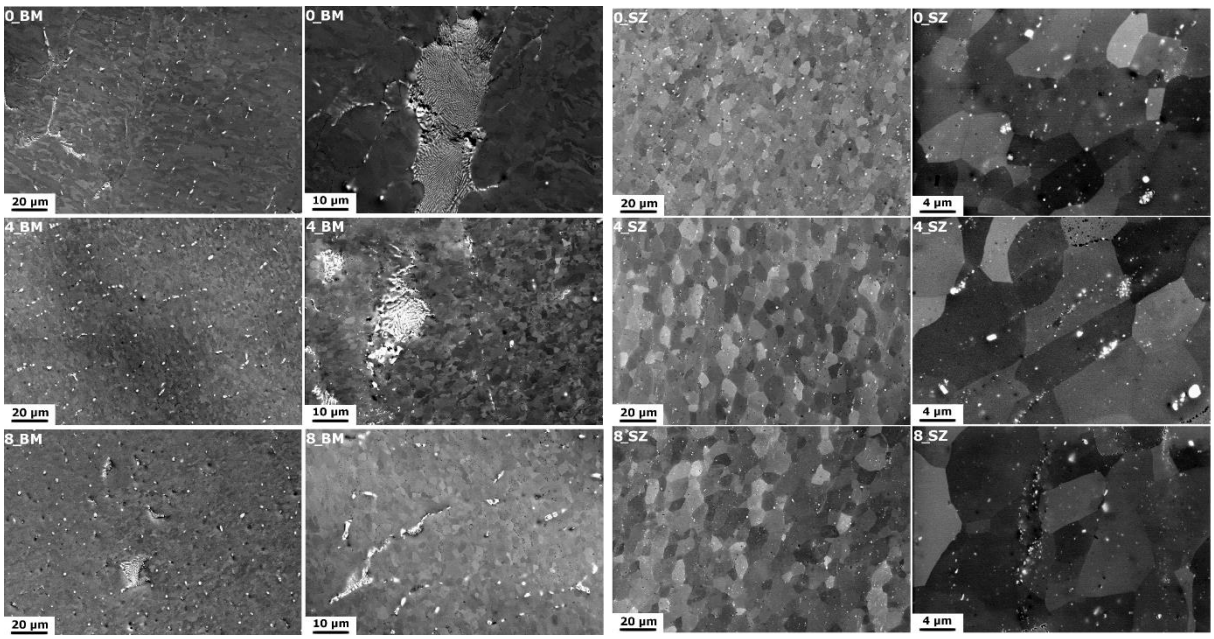

Figure 3. Microstructure of base materials (BM): in an initial state (cold rolled plate – 0_BM) and after different stages of I-ECAP processing (4_BM & 8_BM) and of stir zones.

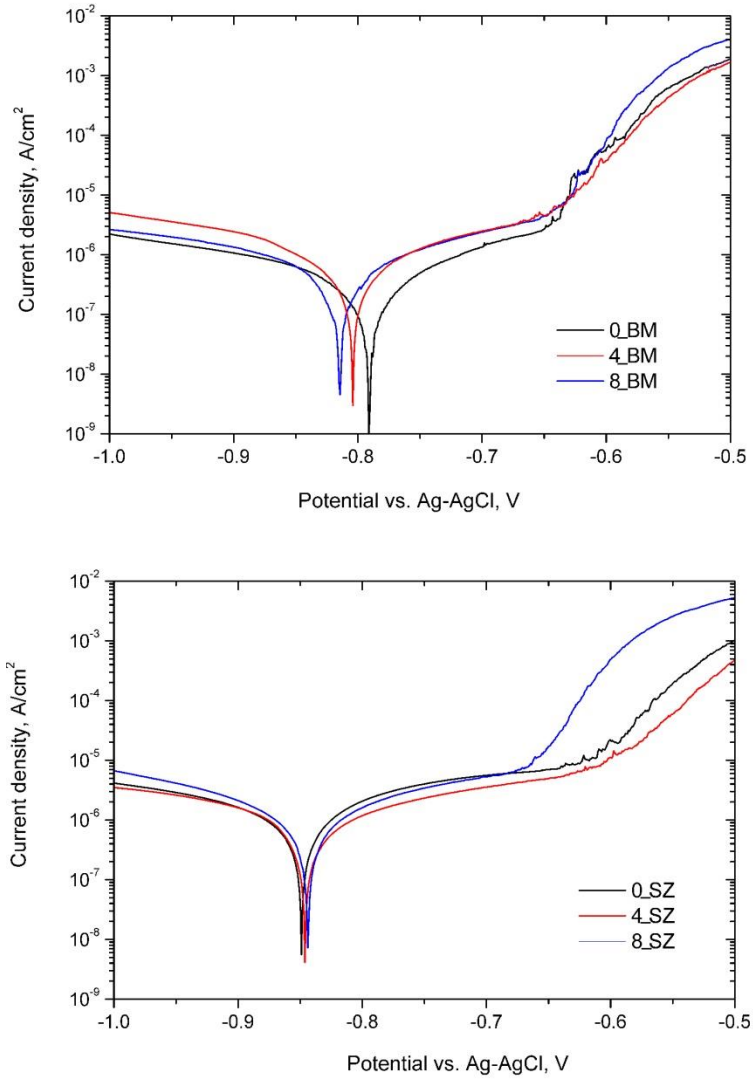

Figure 4. Electrochemical testing for BM (upper diagram) and SZ (lower diagram) samples - potentiodynamic polarization curves recorded in aerated 3.5% NaCl at room temperature.

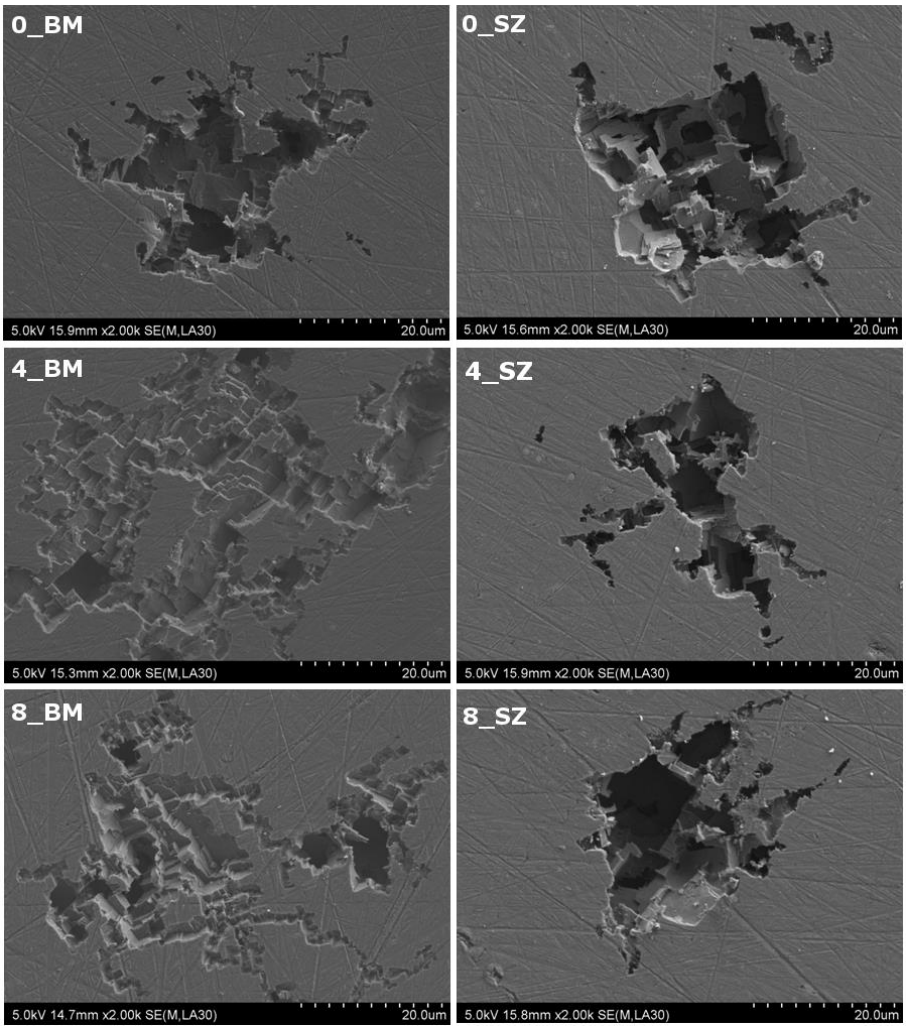

Figure 5. Morphology of corrosion attack after potentiodynamic tests of base materials (BM) and stir zones (SZ); the number indicates the number of I-ECAP passes of the initial material.

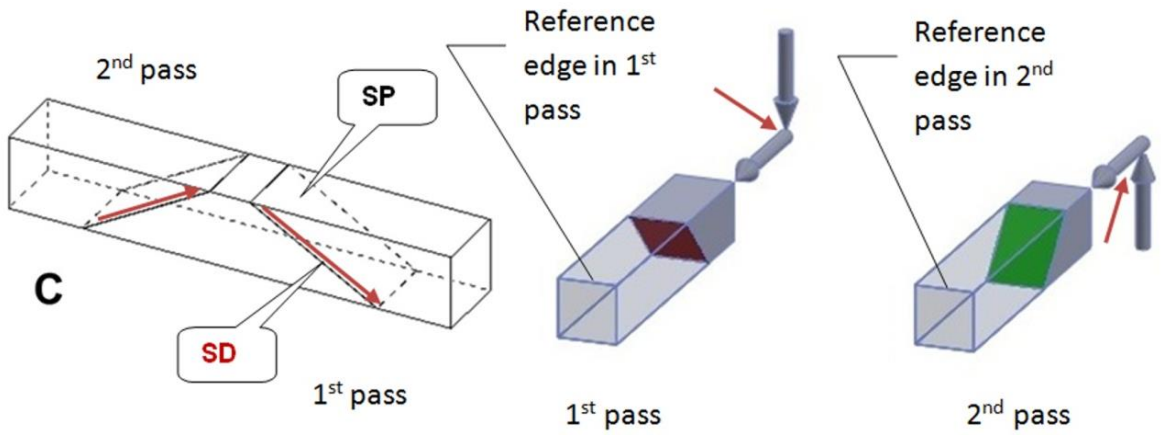

Figure 6. Positions of shear planes SP and shear directions SD in two consecutive ECAP passes in route C and their explanation.

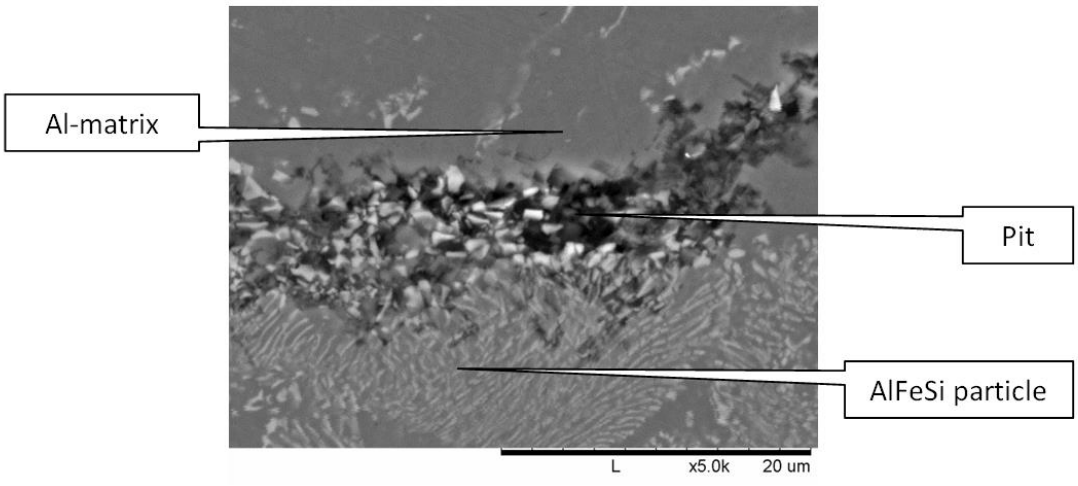

Figure 7. Initiation of pits in the surroundings of AlFeSi particles.

Table 1. Microstructural parameters: average grain size, d_2, grain size distribution, CV(d), shape factor, α, and the fraction of HAGBs for BMs and SZs.

	0_BM	4_BM	8_BM	0_SZ	4_SZ	8_SZ
d_2 [μm]	2.79	1.28	1.16	5.91	6.2	6.25
CV (d)	4.59	1.32	0.79	0.69	0.62	0.62
α	1.43	1.46	1.51	1.41	1.48	1.39
HAGB [%]	2.9	40.5	53.1	62.3	68.1	65.3

Table 2. Stereological parameters describing AlFeSi particles present in the microstructure of base materials (BM) and stir zones (SZ). The number indicates the number of I-ECAP passes.

	0_BM	4_BM	8_BM	0_SZ	4_SZ	8_SZ
d_{2p}[μm]	0.93	0.64	0.47	0.38	0.25	0.13
CV_p (d)	0.40	0.38	0.30	0.14	0.10	0.06
α_p	1.43	1.28	1.27	1.18	1.15	1.15

Table 3. Corrosion potential (E_{corr}), corrosion current density (i_{corr}), pitting potential (E_{pit}), current density at cathodic and anodic range at specific potentials (i_{cath} at -0.95 $V_{Ag/AgCl}$ and - i_{pass} at 0.73 $V_{Ag/AgCl}$); the surface fraction A_A and the number of pits per unit surface N_A.

Sample	E_{corr} [$V_{Ag/AgCl}$]	i_{corr} [$\mu A/cm^2$]	i_{cath} at -0.95 $V_{Ag/AgCl}$, [$\mu A/cm^2$]	i_{pass} at -0.73 $V_{Ag/AgCl}$, [$\mu A/cm^2$]	E_{pit}, [$V_{Ag/AgCl}$]	N_A, [$1/\mu m^2$]	A_A, [%]
0_BM	-0.78	0.5	1.5	0.9	-0.64	$1.2*10^{-3}$	1.84
4_BM	-0.80	1.1	3.7	1.7	-0.65	$2.2*10^{-3}$	3.32
8_BM	-0.81	1.0	2.0	1.7	-0.65	$2.2*10^{-3}$	3.61
0_SZ	-0.84	2.1	2.8	4.5	-0.61	$6.3*10^{-4}$	1.65
4_SZ	-0.85	1.5	2.5	3.0	-0.61	$3.0*10^{-4}$	1.66
8_SZ	-0.84	1.6	3.9	3.9	-0.67	$4.3*10^{-4}$	1.29

Marta Lipińska, Ewa Ura-Bińczyk, Lech Olejnik, Andrzej Rosochowski, Małgorzata Lewandowska*

Microstructure and Corrosion Behavior of the Friction Stir Welded Joints Made from Ultrafine Grained Aluminium

The changes in the microstructure and corrosion resistance between base materials (BM) and stir zones (SZ) were investigated. The number refers to the number of I-ECAP passes of base material. After the corrosion tests the surface of the samples was examined using SEM. With increasing number of I-ECAP passes the pits pose more developed structure with linked cavities. For SZ samples, which exhibit higher grain size, the number of pits is reduced. Pits are also less developed but deeper. The number of pits and surface covered by them is connected with size of AlFeSi particles.